Analysis of DNS and LES of Flow in a Low Pressure Turbine Cascade with Incoming Wakes and Comparison with Experiments

VITTORIO MICHELASSI*, JAN WISSINK and WOLFGANG RODI
Institut für Hydromechanik, Universität Karlsruhe, Kaiserstrasse 12, D-76128 Karlsruhe, Germany

Abstract. The flow around a low-pressure turbine rotor blade with incoming periodic wakes is computed by means of DNS and LES. The latter adopts a dynamic sub-grid-scale model. The computed results are compared with time-averaged and instantaneous measured quantities. The simulations reveal the presence of elongated flow structures, stemming from the incoming wake vorticity, which interact with the pressure side boundary layer. As the wake approaches the upstream half of the suction side, its vortical structures are stretched and align with the main flow, resulting in an impingement at virtually zero angle of attack. Periodically, in the absence of impinging wakes, the laminar suction side boundary layer separates in the adverse pressure gradient region. Flow in the laminar separation bubble is found to undergo transition via a Kelvin–Helmholtz instability. Subsequent impingement of the wake inhibits separation and thus promotes boundary layer reattachment. LES provides a fair reproduction of the DNS results both in terms of instantaneous, phase-averaged, and time-averaged flow fields with a considerable reduction in computational effort.

Key words: DNS, free-stream turbulence, LES, transition, turbine cascades.

1. Introduction

The growing demand for high performance power generation and propulsion systems significantly increased the research effort in the gas turbine field. This effort led to the development of advanced test rigs and computational tools. One of the crucial points to be understood for the optimisation of gas turbines is the stator-rotor interaction phenomenon, which can have a serious impact on the performances of both stator and rotor rows. In this view, experimental and computational analyses evolve from an isolated row towards full-stage or multistage investigations to capture the mutual interaction between rows [9].

Both intensive experimental and numerical investigations have been carried out in the past, especially in the field of Low-Pressure (LP) turbines stages [5, 11, 12, 17], which have attracted much more attention than High-Pressure (HP) turbines [20]. A great effort has been devoted to the development of models able to mimic the effect of unsteadiness in steady flow solvers, like in mixing-plane

---

* On leave from the University of Roma Tre, Italy.

approach [2, 7] without and with deterministic stresses [25], although these models are intrinsically unable to detail the unsteady boundary layer state. A number of unsteady flow solvers designed to study the stator-rotor interaction has been developed [5, 9, 11, 20]. Still, large difficulties in the simulation arise due to the unsteady interaction of the wakes generated by the upstream blade rows with the boundary layers. This interaction is known to cause the intermittent by-pass transition to turbulence of the boundary layers. The simulation of such a complex unsteady environment was tackled by using a number of models based on unsteady Reynolds-averaged Navier–Stokes equations accompanied by one- or two-equation turbulence models, like in [5, 6] eventually coupled with an intermittency transport equation [20]. In off-design conditions the suction side boundary layer is often laminar until it separates due to excessive load [3]. In this case transition, which occurs in the intermittent reverse flow region, was simulated by using the model proposed by Kwon and Pletcher [15] and further modified by Rodi and Schönung [26]. In general, models developed for steady flows, like the by-pass transition model by Abu-Ghannam and Shaw [1], are applied to unsteady flows [20] with no, or minor, modifications. Hence, most of the models still lack a sufficient degree of generality to allow a reliable industrial application to three-dimensional unsteady environments (see [18, 27] for more complete reviews). Further development and testing is necessary, but this requires detailed data which are only partly available from experiments.

Nowadays, Direct Numerical Simulations (DNS) and also sufficiently resolved Large Eddy Simulations (LES) offer the possibility of studying in detail complex turbulent and transitional flows and can provide a wealth of data for developing and testing models. Although a DNS of a full turbine stage is certainly far beyond the capabilities of modern super computers, it is now possible to compute the wake-blade interaction in a single linear cascade at realistic Reynolds numbers, as was done by Wu and Durbin [33]. As part of the German Research Foundation (DFG) project "Unsteady Periodic Flow in Turbomachinery", DNS and also LES calculations of unsteady transitional flow in turbomachinery related geometries were performed with the aim of studying in detail the complex flow phenomena in such situations and of generating data for transition- and turbulence-model improvement and testing. As cascade test case a T106 cascade at a Reynolds number (based on axial chord and inlet velocity) of 5.18×10^4 was chosen for which experiments had been performed by a partner of the DFG project [28, 29]. The DNS of Wu and Durbin [33] were carried out for the same cascade, albeit at a higher Reynolds number of 1.48×10^5 and at a different angle of attack and incoming wake frequency. These authors used as inflow conditions for the incoming wakes data generated from a Large Eddy Simulation of a model problem that mimics the far-field behaviour of a turbulent wake [33, 34]. These wake data were taken over also for the present calculations. The DNS calculations are partly reported already in Wissink [31], where the central theme is the comparison of the present DNS to the DNS performed by Wu and Durbin [33], discussing the effects of different

angles of attack of the oncoming flow, the different angles between the wake axis and the inflow plane and the reduced receptivity of the suction side boundary layer with respect to impinging free stream disturbances because of the lower Reynolds number. Some comparison with the experimental data of Stadtmüller [28, 29] was also included. In the present paper, the comparison of the DNS data with the experiments [28, 29] will be extended and results of additional LES calculations will be presented and discussed with the aim of finding out how close the considerably cheaper LES can reproduce the DNS results. The comparison will also include some results from compressible URANS calculations. The focus of the paper will be the assessments of the LES results *vis-à-vis* the DNS results and their use to analyse the complex unsteady and partly transitional flow fields and provide data for RANS model development.

2. Description of the Test Case

The measurements refer to a low-pressure linear turbine test rig composed of seven aft-loaded blades [28]. The blade aspect ratio (h/c) is 1.76, according to which the assumption of a nearly two-dimensional flow at mid-span appears reasonable. The pitch-to-chord ratio (t/c) is 0.799, which clearly places this blade in the range of mildly loaded LP turbine blades. Since the test-rig allows controlling the fluid density independently of the fluid velocity, it has been possible to perform the measurements at the relatively low Reynolds number of 5.18×10^4 and with an isentropic exit Mach number of 0.4. The stagger angle, γ, inlet angle, β_1, and outlet angle, β_2, are 30.72, 37.7 and 63.2 deg respectively, defined with respect to the axial direction (see Figure 1). The test rig allows simulating the effect of upstream blade rows by a moving bar wake generator with a bar diameter to blade chord ratio of $d_b/c = 0.02$. This system allows producing wakes very similar to those produced by an airfoil, although their strength is probably weaker than that of real IGV wakes. The test rig does not allow to reproduce any sort of static pressure interaction between stator and rotor rows, which might play some role in triggering transition on the front part of the rotor blade. Still, the low-pressure nature of the test indicates that this effect should be mild.

Measurements include the time-averaged distribution of the static pressure around the blade, the time-averaged distribution of the losses in a cross-section downstream of the wake, and the time resolved quasi-wall-shear stress on the suction side of the blade [28].

The experiments had some difficulties in identifying the actual inlet conditions in both terms of inlet flow angle and total pressure. Apparently, the actual inlet flow angle is not 37.7 deg as designed, but 45.5 deg, as suggested by a number of RANS simulations performed by Stadtmüller[28]. The increased inlet flow angle is probably a consequence of the low Reynolds number that causes a migration of the flow towards the bottom of the test rig [28]. Therefore, in both DNS and LES the inlet flow angle was set at 45.5 deg. The inlet total pressure was measured

upstream of the moving bars. This has been taken into account in the blade pressure and wake data.

3. Computational Details

3.1. GRID GENERATION

In accordance with the simulations of Wu and Durbin [33], the grid employed in the DNS and LES was carefully selected using the elliptic grid generation algorithm proposed by Hsu and Lee [13]. Although a multi-block mesh would be the best option (with an O-grid wrapped around the blade and an H-type mesh for the flow core), the elliptic mesh generation ensured a nearly orthogonal (and Cartesian) grid close to the blade walls and it was therefore adopted for the simulations.

The grid employed in the DNS [31] selected for the comparison contains $1014 \times 266 \times 64$ nodes in the stream-wise, pitch-wise, and span-wise directions respectively (see Table I). The grid extension in the span-wise direction and down-stream of the trailing edge is $0.20C_{ax}$ and $1.0C_{ax}$ respectively. A check of the flow structures size resolved by the DNS indicated that a grid with $448 \times 144 \times 32$ points in the stream-wise, pitch-wise, and span-wise directions respectively, would provide a sufficient resolution for LES (see Figure 1). The LES grid extension in the span-wise direction and downstream of the trailing edge is $0.15Cax$ and $0.8C_{ax}$ respectively. Previous experience gained in the simulation of laminar separation bubbles at a comparable Reynolds number [31] showed us that the span-wise exten-sion chosen in the DNS and LES should be sufficient for an accurate simulation of separated flow transition. The uniform grid in the span-wise direction was selected upon the assumption of a homogeneous flow. The grid cell size in wall units was checked in the flow region near the suction side crown of the blade, which is the most demanding in terms of grid resolution. The maximum values of Δx^+, Δy^+, and Δz^+, computed using the value of u_τ on the suction side, are summarised in Table I. These values were considered suitable for providing the necessary resolu-tion of fluid structures. Note that the boundary layer resolving grid near the wall is directly responsible for the relatively large number of grid points employed in the LES, which is only one order of magnitude smaller than the number of grid points employed in the DNS.

The influence of the inlet flow angle was tested by performing a set of prelimi-nary RANS simulations. In this case a coarser 2D grid with 256×144 grid nodes was found to be sufficient to resolve the boundary layer with a fair degree of accu-racy, since the first grid node in the boundary layer was located at approximately $y^+ < 2$ in the laminar region and $y^+ \cong 1$ in the turbulent region.

3.2. CALCULATION METHODS

Both DNS and LES of the flow around the T106 turbine blade have been performed using the LESOCC code [4]. The code discretizes the incompressible continuity
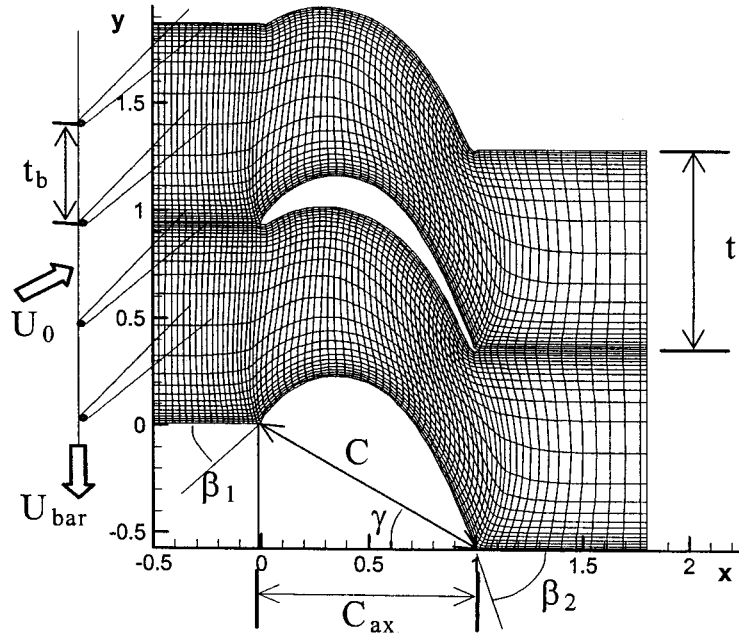
Figure 1. Flow configuration and grid used for LES (every 6 nodes are shown in both stream-wise and pitch-wise directions).

Table I. Overview of the simulations and the grids.

Simulation	Model	Grid	Span size h_s/C_{ax}	Δx^+	Δy^+	Δz^+
DNS	None	$1014 \times 266 \times 64$	0.20	10	0.8	3
LES	Dynamic SGS	$448 \times 144 \times 32$	0.15	28	1.8	6
RANS	k–ω	256×144	–	60	1.9	–

and momentum equations by means of a cell-centred finite volume method. The implicit solution of the Poisson equation for the pressure correction (SIMPLE), originally adopted in [4], is complemented with a Fourier solver in the span-wise direction [19] which substantially reduces the computational effort required to enforce mass conservation. The equations are solved by marching in time with a three-stage Runge–Kutta algorithm. Mass conservation is enforced at the end of each update of the velocities, i.e. after the three Runge–Kutta sub-steps. The Sub-Grid-Scale (SGS) model used in the LES is the dynamic model by Germano et al. [10].

The RANS simulations have been carried out using the compressible XFLOS code [20], which solves the mass, momentum, and energy equations in unsteady conservative form. The effect of turbulence on the mean flow field is accounted

for by using the k–ω turbulence model [30] with the realizability constraint described in [8] to reduce excessive turbulence production in the stagnation region. The onset of transition is detected by using the model proposed by Mayle [18]. The compressible RANS simulations have been used here only to provide a preliminary overview of the flow field. Therefore only a limited portion of these results will be reported; a full account is given in [23].

3.3. BOUNDARY CONDITIONS AND PHASE AVERAGING

All computer simulations enforce a no-slip boundary condition on the blade. The assumption of a periodic flow in the pitch-wise direction is not critical for both DNS and LES since the size of the expected fluid structures is a small percentage of the blade pitch. The periodic boundary condition, enforced also in the span-wise direction, should not alter the development of stream- and span-wise flow structures. The values of h_s/C_{ax} given in Table I were deemed suited to meet this requirement [31, 33].

The incoming wakes at the inflow boundary employed in the LES are enforced in the same way as in the DNS, using the data base which has been kindly made available by Wu and Durbin and is described in [34]. In the current simulations the wake half-width and maximum wake deficit were $0.03C$ and 25% respectively. The wake pitch is 1/2 of the blade pitch (see Figure 1), and the non-dimensional tangential velocity of the wake was $u_{\text{bar}} = 0.41$. These values have been selected in order to fit the experimental incoming wakes described by Stadtmüller [28] for the T106 blade measurements.

In order to properly resolve the wake in both space and time, one period $T = t_b/U_b$, i.e. a half-blade-pitch sweep of the wake, was resolved using 9600 time steps in the DNS, 4800 time steps in the LES, and 60 time steps in the RANS. For both DNS and LES this choice implies a maximum CFL number of approximately 0.30–0.50, while in RANS the CFL number was set to 15. Like in the DNS [31], in the LES the flow was allowed to develop for five periods T. Once time-periodic flow had developed, phase-averaging was carried out for 10 periods. While in the DNS each wake passage (equal to one period T) was subdivided into 240 phases, because of memory restrictions in the LES "only" 120 phases were stored. This was found to be sufficient to obtain a detailed description of the flow evolution in time. In the following, t/T is used to identify instantaneous flow fields, while Φ, with $0 \leq \Phi < 1$, corresponds to the phase of a phase-averaged flow field.

4. Analysis of Time-Averaged Quantities

4.1. STATIC PRESSURE DISTRIBUTION AROUND THE BLADE

The computation of the time-averaged static pressure coefficient, C_p, requires the total pressure, $p_{0-\text{in}}$, immediately downstream of the wake generator, which is controlled by the loss mechanism induced by the moving bars. The uncertainty in

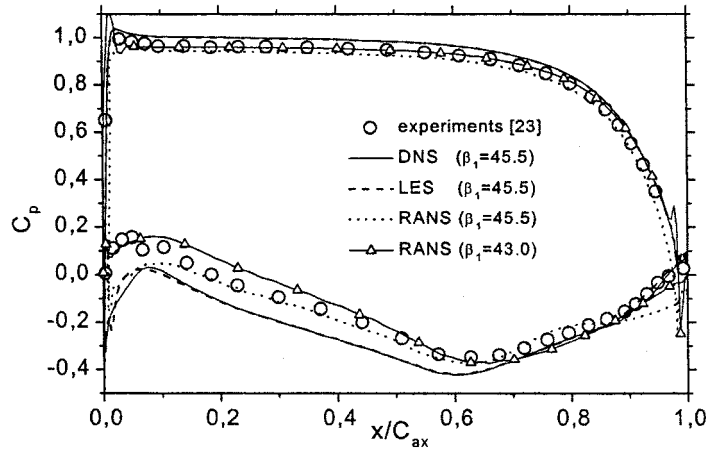*Figure 2.* Time-averaged static pressure coefficient distribution around the blade.

$p_{0-\text{in}}$ is addressed by Stadtmüller [28] who defines C_p as $(p_w - p_{\text{ref}})/(p_{0-b} - p_{\text{ref}})$, where p_{ref} is the reference exit static pressure, p_w is the blade wall static pressure, and p_{0-b} is a corrected inlet total pressure which accounts for the total pressure reduction due to the bar-induced losses. With this definition, the time-averaged static pressure computed by DNS, LES, and RANS is compared with the test-rig values in Figure 2. Following the suggestion of Stadtmüller [28], the inlet flow angle was set to 45.5 deg instead of the design value of 37.7 deg. This angle, however, produces an excessive blade load, especially on the suction side in proximity of the leading edge for DNS, LES and RANS (see Figure 2). A further RANS simulation showed that the static pressure coefficient could be predicted in better agreement with the experiments by setting $\beta_1 = 43.0$ deg (see Figure 2). Figure 2 shows that the DNS and LES results are almost indistinguishable. The shift between the measurements and both DNS and LES stems from the incompressible nature of the simulations. In fact, both DNS and LES results fit the exit static pressure and capture the overall trend very well, but deviate from the data on the suction side where the local isentropic Mach number exceeds 0.40–0.45 (as shown in the compressible RANS results with $\beta_{\text{in}} = 43$ deg displayed in Figure 3). In this velocity range, the local density variation with respect to the inlet total density is of the order of 5–10%, which, together with the experimental uncertainty in the inlet flow angle, may well be the cause of the discrepancy in the pressure coefficient along the upstream half of the suction side observed in Figure 2.

4.2. WAKE LOSSES

The total pressure losses in the linear cascade are monitored using the so-called kinetic loss coefficient, ω, defined as $\omega = (p_{0-\text{inlet}} - p_{0-\text{exit}})/(p_{0-\text{inlet}} - p_{\text{ref}})$. The total pressure $p_{0-\text{exit}}$ is taken at a plane located at $0.4C_{ax}$ downstream of the
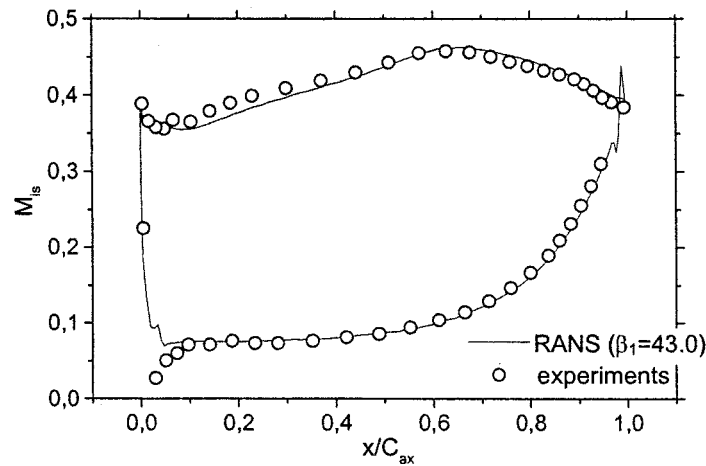
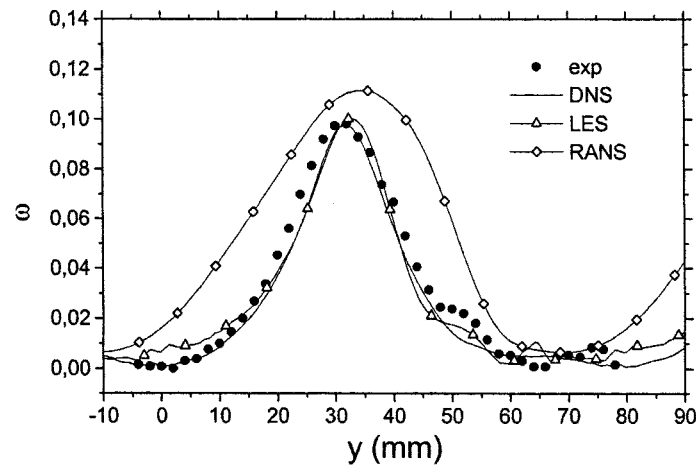*Figure 3.* Time-averaged isentropic Mach number distribution around the blade.

Figure 4. Kinetic loss coefficient $40\% C_{ax}$ downstream of the trailing edge; (pitch is 80 mm).

trailing edge. Although this is often addressed as the "profile" loss coefficient, in this case it includes also the mixing losses occurring from the trailing edge to the measurement plane. In Figure 4 the measured kinetic loss coefficient distribution in the pitch-wise direction is compared with DNS, LES, and RANS. All the reported values are time averaged. The measured wake is shown to be quite thick, and the losses quite large, thereby illustrating the heavy off-design conditions at which the blade is operated. The DNS and the LES match the experimental result very well, although the losses predicted by LES are slightly overestimated away from the wake. RANS overestimates the losses and the wake width. This is partly due to the quite coarse grid adopted in the stream-wise direction and partly to the turbulence model (see further elaboration in [23]).
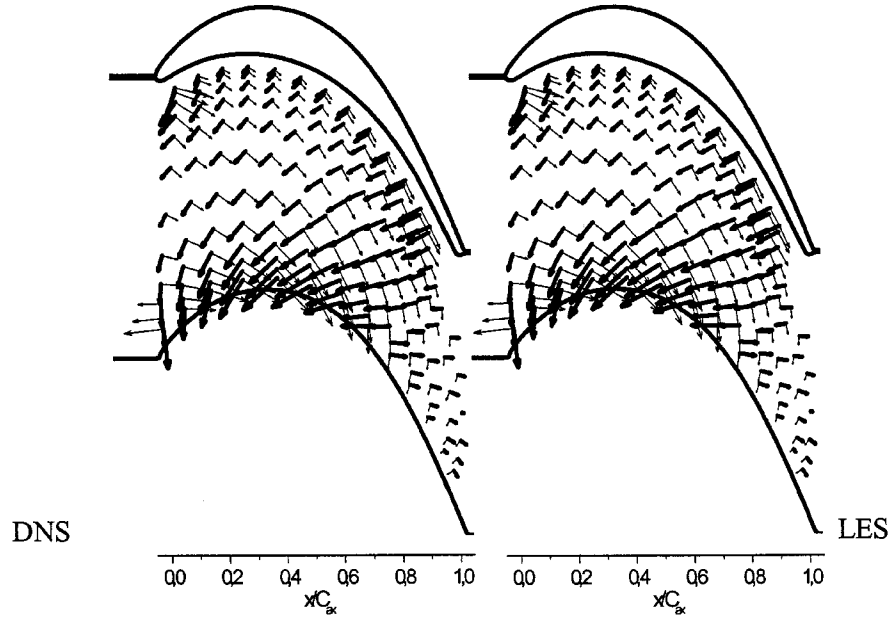
Figure 5. Principal axes of the mean strain tensor. Vector length proportional to tensor eigenvalues. (σ_1 = thin arrow – direction of stretching, σ_2 = thick arrow – direction of compression).

4.3. PRINCIPAL AXES OF STRAIN TENSOR

Some features of the flow field are better understood when looking at the principal axes of the mean strain tensor plotted in Figure 5. The principal axes, σ_1 and σ_2, correspond to the eigenvectors of the two-dimensional rate of strain tensor

$$S_{i,j} = \frac{1}{2}\left(\frac{\partial u_i}{\partial x_j} + \frac{\partial u_j}{\partial x_i}\right)$$

of the time-averaged flow field. Since the eigenvectors and eigenvalues change only very little in time, the use of phase-averaging was discarded. Following the analysis proposed by Wu and Durbin [33], σ_1 identifies the direction along which the mean flow is stretched, whereas σ_2 corresponds to the direction of compression. The eigenvectors σ_1 and σ_2 are normalised such that their length corresponds to the value of their respective eigenvalues, and therefore indicates the strength of the stretching/compression.

The principal axis which identifies the direction of stretching is almost aligned with the pressure side wall, although the intensity of stretching becomes relevant only in the second half of the vane ($x/C_{ax} > 0.5$). When moving towards the suction side, it is the direction of compression that aligns with the blade in the immediate proximity of the leading edge. When proceeding further downstream ($0.1 < x/C_{ax} < 0.6$) the flow first aligns with the direction of stretching across

the entire section, while for $x/C_{ax} > 0.6$–0.65 the flow in proximity of the suction side is marginally compressed. In general, Figure 5 illustrates that the DNS and LES time-averaged flow fields are virtually identical.

5. Visualisation of Unsteady Flow and Flow Structures

Jeong and Hussain [14] showed that local vortical structures can be identified using iso-surfaces of negative values of the second largest eigenvalue, λ_2, of $S^2 + \Omega^2$, where S and Ω are the symmetric and anti-symmetric parts of the velocity gradient tensor, respectively. For the computation of λ_2 the instantaneous velocity field was used. Figure 6 refers to the LES, the DNS plots [31] look very similar and are therefore omitted. The four phases illustrate how the wake is gradually swallowed in the vane and turned counter-clockwise in the upper part. As observed in the larger Reynolds-number case [33], the approaching wake does not show any preferential vortex direction as long as it does not feel the pressure gradient.

As soon as the blade curvature provokes a strong flow acceleration, the portion of the wake closer to the pressure side aligns with the principal axis that identifies the direction of stretching (see also Figure 5). This phenomenon concentrates streamwise vorticity both in the present case at Re $= 5.18 \times 10^4$ and at Re $= 1.48 \times 10^5$ [33], the consequence of which is the development of elongated vortical structures visible in Figure 6. Figure 7 compares the axial vorticity iso-surfaces, visible as tube-like vortical structures in the proximity of the pressure side, for both DNS and LES.

To facilitate the understanding of the overall flow development, Figure 7 also shows the span-wise vorticity on a plane orthogonal to the blade, which allows a clear detection of the wake position in the vane (see the black arrows). The flow acceleration and turning is found to align the upper portion of the wake with the blade pressure side. The vortical structures are mildly elongated as long as the static pressure is substantially constant, while, for $x/C_{ax} > 0.6$–0.7 the strong flow acceleration on the pressure side provokes a strong vortex straining, as the wake is aligned with the direction of stretching. Figure 7 shows that the LES captures the size and shape of the structures convected by the wake with fair accuracy compared to DNS.

Compared to what was observed by Wu and Durbin [33], in the lower Reynolds number simulations the pressure side is continuously affected by the vortices because the incoming wake frequency is twice as high. Apparently, the wake vortices gradually approach the blade pressure side until they manage to enter the boundary layer. Figure 8 shows that the elongated vortical structures gradually reduce in size while approaching the pressure side. A similar pattern was discovered in the DNS [31]. It can be attributed to the proximity of the solid wall which limits the size of the structures. The strong acceleration of the flow core on this side of the blade is responsible for the virtual absence of any significant turbulence activity.
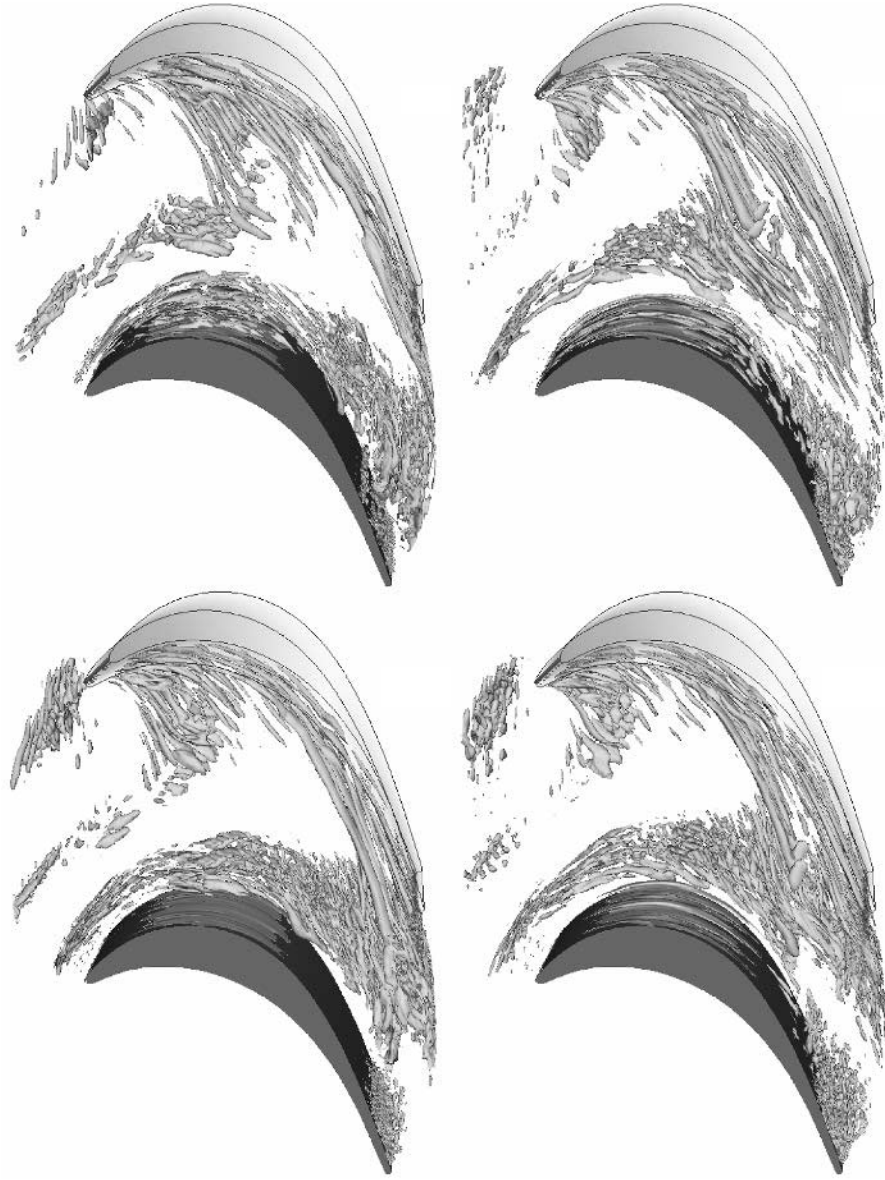
Figure 6. LES: Instantaneous λ_2 iso-surfaces ($t/T = 15.00, 15.25, 15.50, 15.75$ from top-left clockwise).
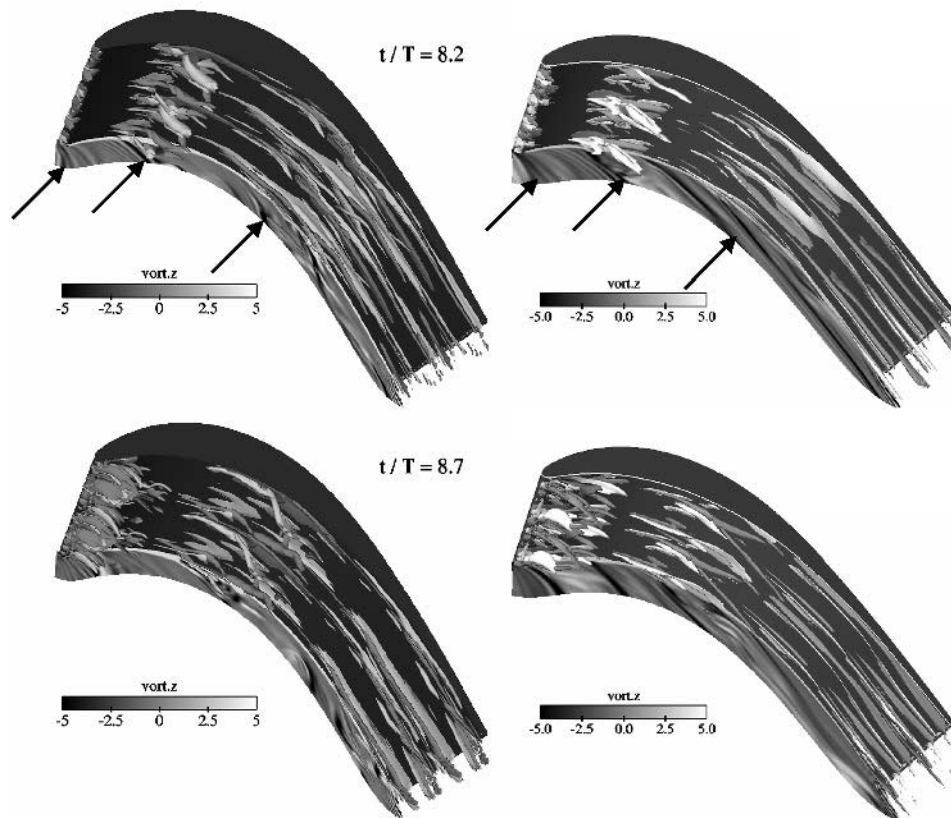
Figure 7. Instantaneous iso-surface of axial vorticity in proximity of the ps. The blade-normal plane shows the spanwise vorticity (left: DNS, right: LES).
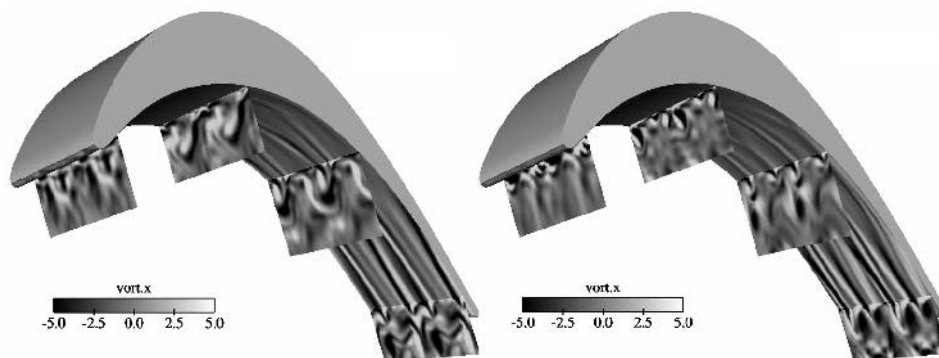

Figure 8. Axial vorticity predicted by LES along the pressure side in four cross-flow planes ($t/T = 8.2$ left, $t/T = 8.7$ right).
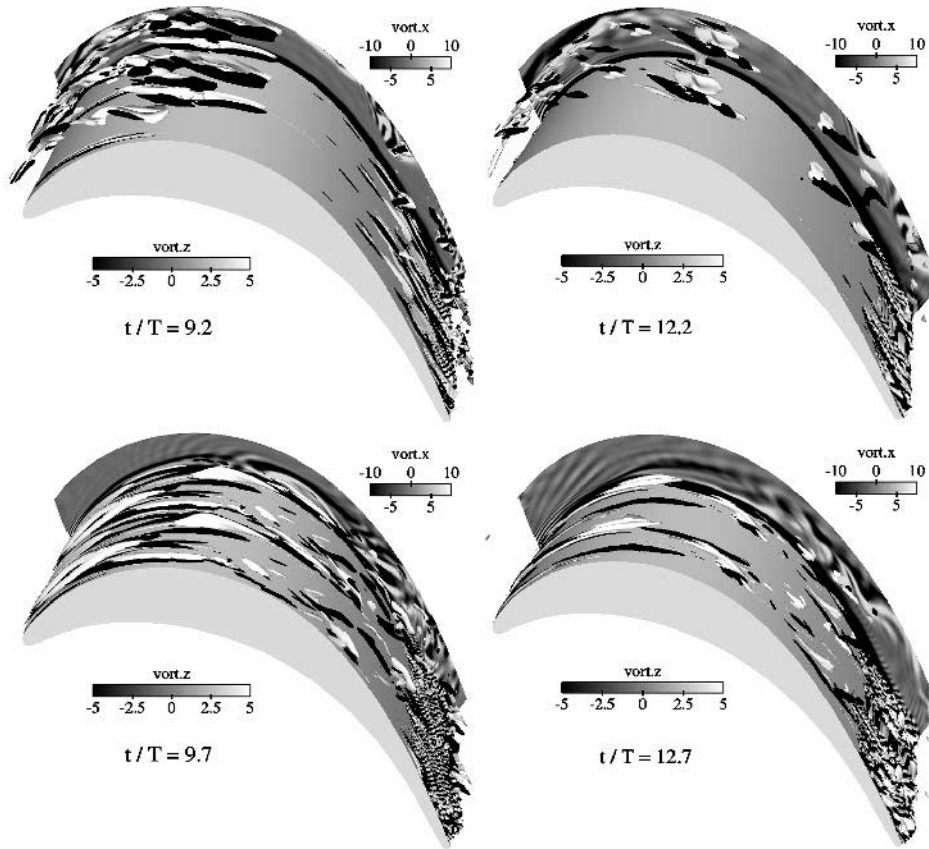
Figure 9. Instantaneous iso-surface of axial vorticity on ss. The blade-normal plane shows the span-wise vorticity (left: DNS, right: LES).

The elongated vortices do not manage to trigger turbulence in the pressure side boundary layer, which remains substantially laminar until the trailing edge.

Comparing Figure 7 to Figure 9 illustrates the considerable differences between the pressure and suction side boundary layers. In the portion of the suction side between the leading edge and $x \cong 0.7 \times C_{ax}$, the boundary layer does not experience strong disturbances. Because of the turning of the wake when it approaches the upstream half of the suction side, the wake impinges at virtually zero angle of attack. Due to the strong acceleration of the flow near the suction side, as in the DNS [31], in the LES no significant turbulence activity is found upstream of $x \cong 0.8C_{ax}$. Figure 9 clearly illustrates the presence of small scale turbulent structures further downstream near the trailing edge on the suction side. As expected, due to the different grid resolution, the LES results show less structures than the DNS results [31].

Figure 10 illustrates how the streamwise vortices affect the suction side boundary layer by showing the axial vorticity in four cross-sections. The size of the
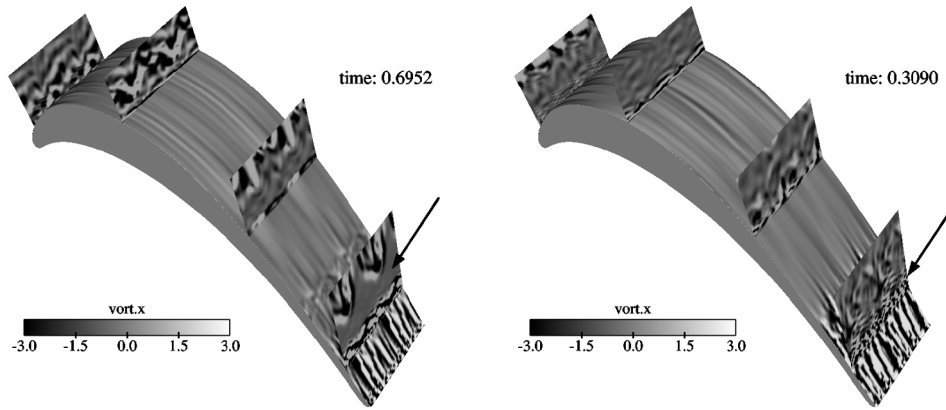
Figure 10. Axial vorticity predicted by LES along the suction side in four cross-flow planes ($t/T = 8.2left, t/T = 8.7$ right).

vortices in proximity to the leading edge is slightly smaller than on the pressure side, probably due to the straining effect of the favourable pressure gradient. In the left figure the wake has not yet reached the blade suction side, as witnessed by the turbulence-free layer pointed by the arrow. The layer close to the wall shows relatively large structures, which are linked to the presence of flow separation which will be discussed in the following sections. Once the effect of the wake is felt, the cross-section in the aft part of the blade reveals the presence of smaller turbulent structures, indicated by the arrow, which trigger the boundary layer state.

Figures 11 and 12 show instantaneous stream traces on the suction and pressure sides respectively, together with the position of the instantaneous separation and the stagnation point. On the suction side the flow is almost aligned with the axial direction and the chaotic streamtraces visible for $x/C_{ax} > 0.8$ are due to a local separation bubble induced transition. On the pressure side the large and elongated flow structures originally described by Wu and Durbin [33] and also observed by Wissink [31] are found to be resolved in the present LES too; they give rise to the peculiar plot of Figure 12. This figure shows evidence of some interaction between the counter-rotating tube-like structures, which provoke local accumulation, or defect, of momentum in the span-wise direction due to a moderate span-wise migration of the axial vorticity cores.

6. Analysis of Phase-Averaged Quantities

6.1. SELECTED PHASES

Figure 13 shows contours of the phase-averaged normal Reynolds stress in the axial direction at three phases, $\phi = 0$, $\phi = 0.4$, and $\phi = 0.8$. This quantity was selected because it is a good measure of the position and strength of both the incoming and blade wakes and it gives contours similar to the turbulent kinetic energy. The
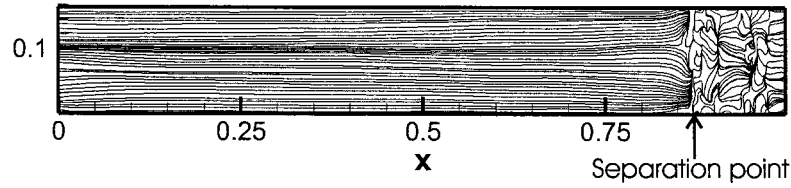
Figure 11. LES: Instantaneous stream-traces on the suction side of the blade, vertical direction is blade span ($y^+ \cong$ 2–5).
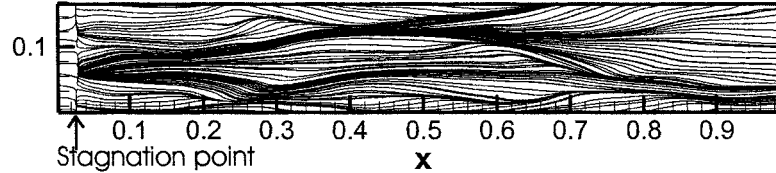

Figure 12. LES: Instantaneous stream-traces on the pressure side of the blade, vertical direction is blade-span ($y^+ \cong$ 1–3).

plots show how the upper part of the wake is first rotated counter-clockwise due to the strong acceleration on the suction side with respect to the pressure side, while the lower part which is closer to the suction side rotates clockwise while aligning with the blade wall. This is a well-known phenomenon in stator-rotor interaction and was described already by several authors in the past [5, 6, 22, 33]. Still, the difficulties in performing measurements in this critical flow region prevented a clear description of the process. In fact most of the experimental work done so far does not include a detailed description of the wake shape in the vane, while most of the numerical work, being carried out by RANS, is still subject to some degree of uncertainty.

The first conclusion that can be drawn from Figure 13 is that DNS and LES give very similar pictures and an almost identical evolution of the wake in the blade vane. In the DNS plot for $\Phi = 0.0$, two of the incoming wakes are labelled. The degree of wake rotation is obviously the same for DNS and LES since it is mainly controlled by convection in the (nearly potential) core flow region. The LES plots only show the resolved fluctuations without any contribution from the SGS model. Part of the differences in the axial velocity fluctuation levels predicted by DNS and LES may be attributed to this, although the instantaneous eddy viscosity given by the SGS model never exceeded 2–3 times the molecular viscosity. Observe that in both the flow regions labelled "1" and "2" the instantaneous eddy viscosity predicted by the SGS model is approximately twice as large as the molecular one. This implies that the SGS model only plays a minor role because the grid employed in the LES provides quite a good resolution. Nevertheless, the fluctuation levels predicted by DNS are undeniable larger, especially in the region of the blade wake, where the higher resolution of the DNS grid plays a significant role.
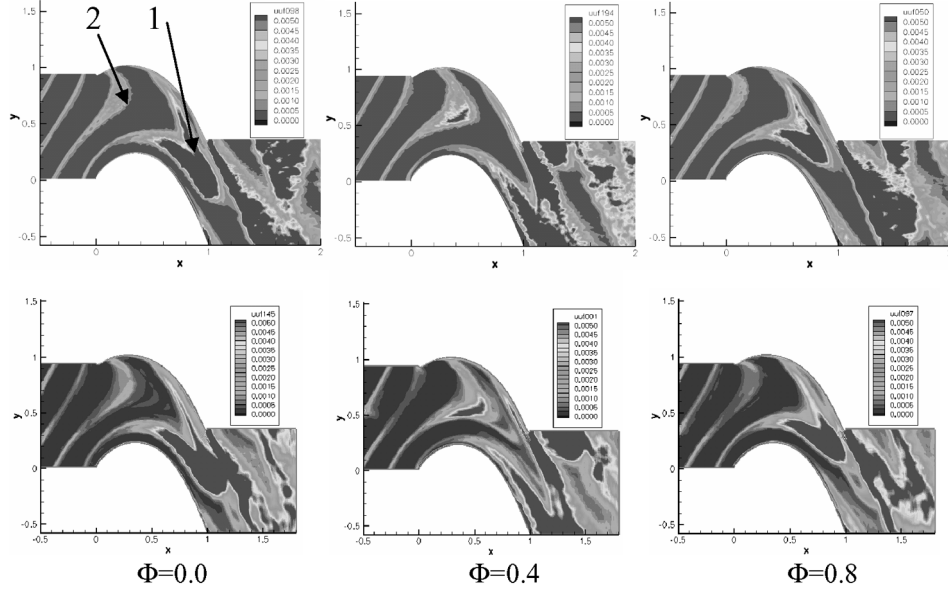
Figure 13. Three phase-averaged snapshots of the axial velocity fluctuation (top DNS, bottom LES).

The way the large velocity fluctuations convected by the wake merge together with the blade wake is interesting and should be studied further. Apparently, the large turbulence area of the flow interacts with both the suction and pressure sides of the blade. In fact, for $\Phi = 0.0$ the plots show that the wake apex first reaches the pressure side of the blade wake, and only later ($\Phi = 0.4$) it manages to mix also with the suction side portion of the blade wake, thereby filling the full blade pitch. This phenomenon may be highly case dependent since it is probably sensitive to the inlet flow angle and the suction side boundary layer state which, under the present operating conditions, undergoes late and incomplete transition (see the shape factor plot in Figure 23). When moving further in time, at $\Phi = 0.8$, the mixing process is almost complete and most of the incoming wake effect has been dissipated.

6.2. CROSS-SECTIONS

A more quantitative comparison between the predictions of DNS and LES is given by the following phase-averaged cross-section plots. Six sections have been selected on the suction side of the blade, ranging from 10% up to 99% of the axial chord. Figure 14 shows how the sections are placed and oriented (approximately orthogonal to the blade surface). For each section, 10 phase-averaged profiles are extracted and compared ($\Phi = 0$ to 0.9, step 0.1). The monitored quantities are the velocity magnitude, u, the turbulent kinetic energy, k, the turbulent shear stress, $\overline{u'v'}$, and the span-wise velocity fluctuation, $\overline{w'w'}$, which was selected to illustrate
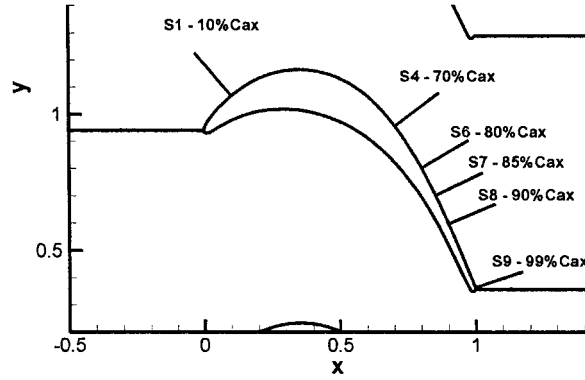
Figure 14. Positions of the 10 cross-sections in the blade vane.

the three-dimensionality of the turbulence field. The abscissas report quantities made non-dimensional with respect to the inlet velocity, while the ordinate gives the distance from the wall. The profiles extend up to a distance of $0.06C_{ax}$ from the wall (which corresponds roughly to 6.4% of the pitch) to provide a zoomed view of the boundary layer in the proximity of the suction side-wall. Each figure contains four plots with 11 curves. The leftmost curve is the time-averaged profile of the variable considered (labelled "A"), while the remaining 10 curves refer to the 10 phases. This extensive comparison is presented in Figure 15. Section 1, located at $0.10C_{ax}$, reveals that both the DNS and LES predict profiles which are very weakly affected by the passing wakes in the front part of the blade. An extensive analysis of the profiles along cross-sections up to 60% of the axial chord [22], not reported here, shows the relative insensitivity of the boundary layer to the incoming wakes. This is most likely due to the strong acceleration of the flow on the suction side which extends up to 55–60% of the axial chord. The flow acceleration produces a severe stretching of the flow that prevents the growth of any significant turbulent fluctuations, as visible in the plots of k, $\overline{u'v'}$, and $\overline{w'w'}$. This first section also shows that the results obtained by DNS and LES are quite similar. The LES profiles shows wiggles in the immediate proximity of the suction side near the leading edge. Even in the DNS small wiggles are found in this region. The most likely cause of these wiggles are instabilities generated by a small leading edge separation bubble (see also [31]) just upstream of this location. Due to the strong flow acceleration upstream of the leading edge separation bubble, the disturbances quickly damp out and do not affect the boundary layer further downstream.

The boundary layer in the front part of the blade is quite insensitive with respect to the impinging disturbances convected by the wakes. This is apparently in contrast with what was found by Liu and Rodi [16] who investigated the effect of incoming wakes over a flat plate boundary layer at a unit Reynolds number, $Re = u \times 1/\nu$, of 9.9×10^5. In their case, although the strength of the wakes was comparable to that of the T106 blade case, the disturbances carried by the

wakes were able to alter considerably the state of the boundary layer already from the leading edge. This difference is most likely caused by the absence of flow acceleration and by the flat nature of the boundary layer. In fact, in a further set of measurements of the flow in a low speed turbine inlet guide vane with incoming wakes and reduced flow turning with respect to the T106 blade, Liu and Rodi [17] measured velocity profiles and boundary layer integral parameters. The measurements do not cover the first 34% of the blade, where the largest acceleration is expected. It is shown how the variations in time (triggered by the incoming wakes) of the velocity, turbulence-quantities, and integral parameters are small in the first 67% of the blade, but subsequently increase downstream towards the trailing edge as in the present case.

When moving further downstream along the suction side of the T106 blade, the pressure gradient slowly becomes adverse. This has an immediate effect on the suction side profiles. In fact, although the plots do not show any significant turbulence activity, the velocity profiles show a weak inflection point (see section S-4) which is evident at all phases in section S-6, regardless of the incoming wake position. The boundary layer thickness profiles displayed in Figure 25 show that up to 60–70% of the axial chord the suction side boundary layer thickness stays constantly below $0.02C_{ax}$–$0.03C_{ax}$, while it rises further downstream. At $x/C_{ax} = 0.8$ no significant turbulence activity is found in either the DNS nor the LES, despite the local increase in boundary layer thickness and the presence of an inflection point. Section 7 shows first signs of flow separation (see for example $\Phi = 0.2$). The good agreement between LES and DNS indicates that the near wall resolution of the LES-grid allows for an accurate prediction of the location of separation. The plots of the turbulence quantities also indicate that the fluctuating components of the velocity are virtually zero for both LES and DNS. This is a clear indication of a laminar separation bubble, the pulsating nature of which triggers the further development of the boundary layer, as it is visible in the plots for the cross-sections 8 and 9. Up to this point, none of the profiles did show any significant difference between the LES and DNS.

The build-up of turbulence in the following sections reveals some differences between DNS and LES. Section 8 shows that the separation bubble is intermittently present (see for example $\Phi = 0.2$–0.4–0.9). The velocity and turbulent shear stress profiles predicted by the LES are in very good agreement with the DNS for all phases. Both the turbulent kinetic energy and the turbulent stress component aligned with the span-wise direction of the two simulations are very similar.

In section 9 the boundary layer thickness has significantly increased (approximately $n/C_{ax} = 0.020$–0.025 in section 8, and 0.030–0.040 in section 9, which corresponds to 2.2–2.7% and 3.2–4.3% of the blade pitch respectively). In section 9 the turbulent kinetic energy obtained with the DNS can reach values twice as high as those predicted by LES, especially when the wake manages to diffuse some micro-scale velocity fluctuations into the boundary layer (see $\Phi = 0.2$–0.3–0.4–0.5). This phenomenon is lost by the LES. Despite the differences in the
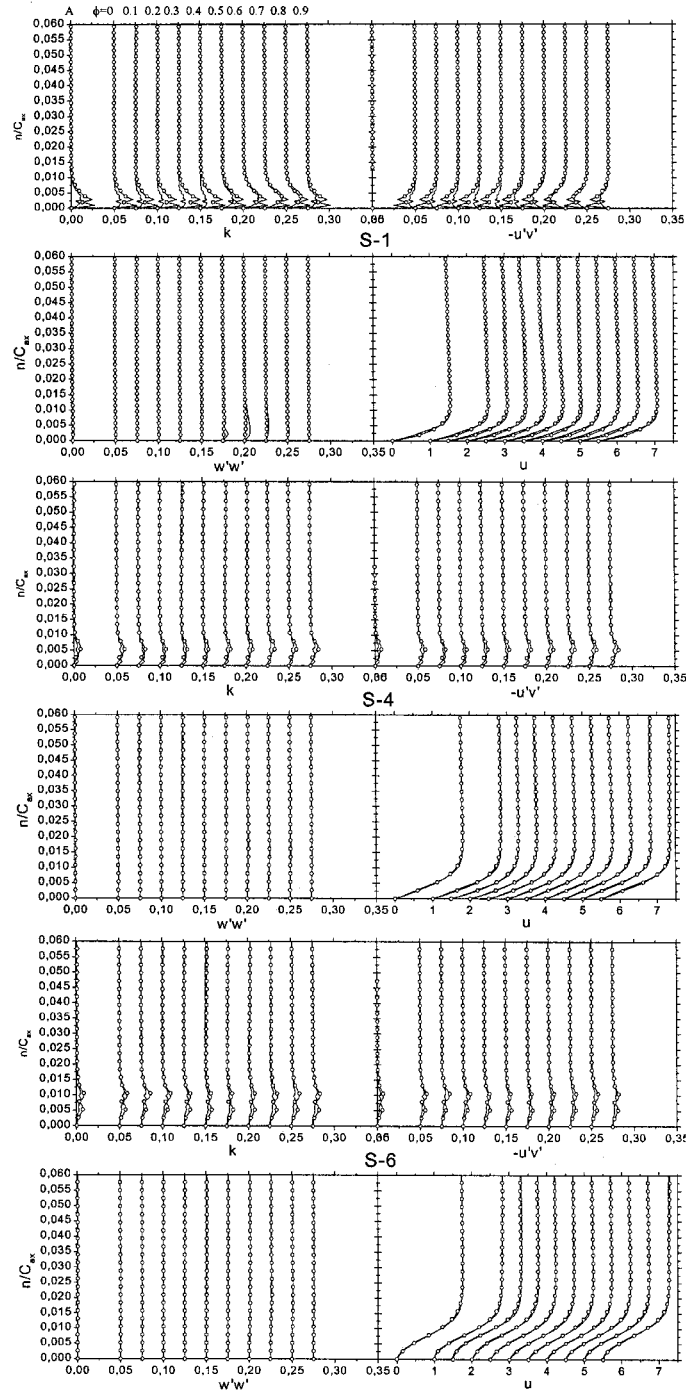
Figure 15. Phase-averaged profiles at 6 cross-sections in the blade vane; from left to right: time-averaged, phase-averaged $\Phi = 0$ to 0.9, step 0.1 (solid line: DNS, solid line+symbols: LES).
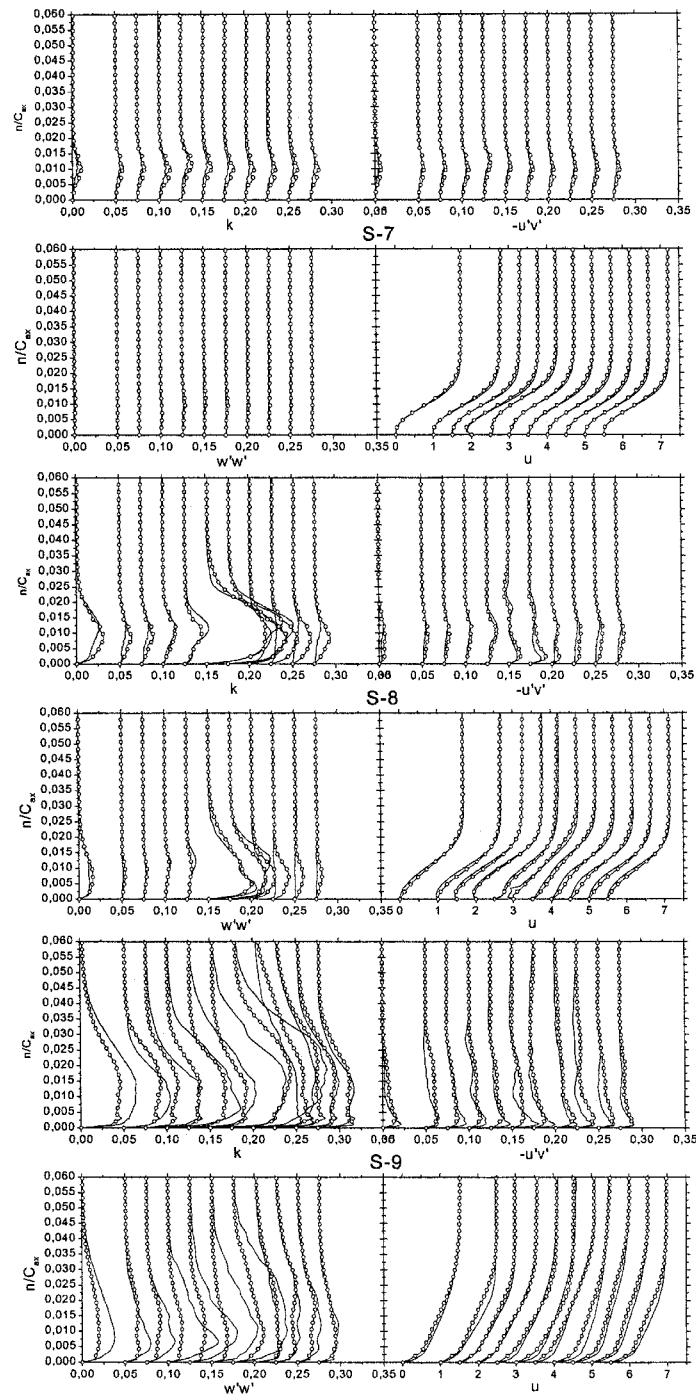
Figure 15. (Continued)

levels of k, the LES manages to capture the build-up of turbulence which is clearly becoming fully three-dimensional, as illustrated in the profiles of the span-wise velocity fluctuations.

The cross-comparison of Figures 13 and 15 suggests that the large values of turbulent kinetic energy at section 9 are not diffused, but triggered by the incoming wakes, which never merge completely with the suction side boundary layer. In this respect the differences between DNS and LES might stem from the lower resolution of the incoming wakes in the flow core provided by the LES grid, which cuts off some of the structures convected by the wakes (see Figure 9) so that their impact onto the suction side boundary layer is diminished. Part of the differences may also be due to the fact that the LES profiles report only the resolved fluctuations without the contribution of the SGS model.

The phase-averaged profiles allow to conclude that DNS and LES give similar flow pictures for all the phases, with differences during some phases at sections 8 and 9. The cross-comparison of the mid-span plots of Figure 13 and the cross-sections of Figure 15 also indicate that both the details of the boundary layer on the suction side and the overall incoming wake diffusion process are fairly similar in the two simulations.

6.3. STATIC PRESSURE AND WALL SHEAR STRESS ON THE SUCTION SIDE

The aerodynamics of the suction side of low speed turbine blades largely controls the overall loss mechanism. Therefore, this paragraph presents the phase-averaged plots of both the static pressure and the wall shear stress along the suction side surface to provide additional insight into this critical flow region. The plots compare the results of the DNS and LES and, where available, experiments. Figure 16 shows the computed static pressure made non-dimensional with the inlet dynamic head. The plots refer to the same 10 phases, equally spaced in time, used in the previous analysis. In the first part of the blade ($x/C_{ax} < 0.8$) not much is happening, despite the presence of the periodically oncoming wakes. This was already noted when analysing the cross-sections of Figure 15. In fact, as long as the pressure gradient remains favourable all the disturbances transported by the wake are damped and do not manage to enter the boundary layer. This is even more evident in Figure 11, which shows the instantaneous stream traces on the suction side of the blade; the shape of the streamlines is virtually unaffected by the passing wakes, and the flow distortion visible at $x > 0.8$ refers to an unsteady separation bubble observed in the previous section. So, it is not surprising that the pressure traces are insensitive to the passing wakes, at least up to an axial position slightly downstream of the location of the first appearance of an adverse pressure gradient. Figure 16 also illustrates the size of the leading edge separation: although both DNS and LES predict a reverse flow region, the former shows a longer bubble which reattaches due to the favourable pressure gradient. Despite the different size, most likely caused by superior grid resolution in the DNS, the bubble does not seem to affect the
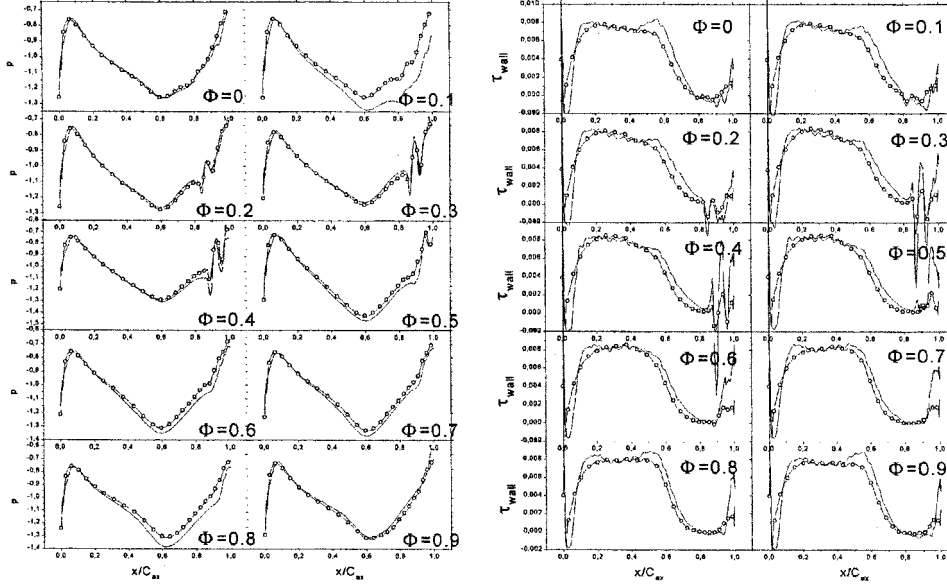
Figure 16. Phase-averaged static pressure and wall shear stresses on blade suction side (solid line: DNS, symbol+solid line: LES).

development of the boundary layer further downstream, probably on account of the strong flow acceleration.

From $\Phi = 0.1$ to 0.4 the pressure plots show an up-down shape at around $x/C_{ax} = 0.9$. This is clearly linked with the observed onset of separation as is made evident by the wall shear stress plots on the right. The two peaks of negative wall shear stress that are found for $\Phi = 0.1$ to 0.4, correspond to the presence of two separation bubbles. These bubbles begin to grow almost simultaneously at $\Phi = 0.1$ when the cross-sections show no significant turbulence activity and the wake reaches the suction side of the blade. Apparently, the separation bubble appears in a laminar-like flow. The further growth of turbulence energy, and the diminished effect of the wake, promote the reattachment of the flow, as visible for $\Phi > 0.5$ in both the pressure and wall shear stress profiles in which the up-down patterns have disappeared. Both the wall shear stress profiles, as well as the pressure profiles predicted by DNS and LES on the suction side are very similar. Nevertheless, during the simulations it was observed that the inlet/outlet pressure fluctuations as predicted by LES may be somewhat wider than those given by DNS. Although this phenomenon still lacks a definite explanation, it might stem from the slightly shorter length of the computational domain downstream of the trailing edge adopted in LES $(0.8C_{ax})$ against DNS $(1.0C_{ax})$.

The experimental data set [28] includes the time resolved quasi-wall-shear-stress, τ_w^*, on the suction side of the blade in the 27 locations shown in Figure 17. The measurements detect the flow separation, but not the magnitude of the wall
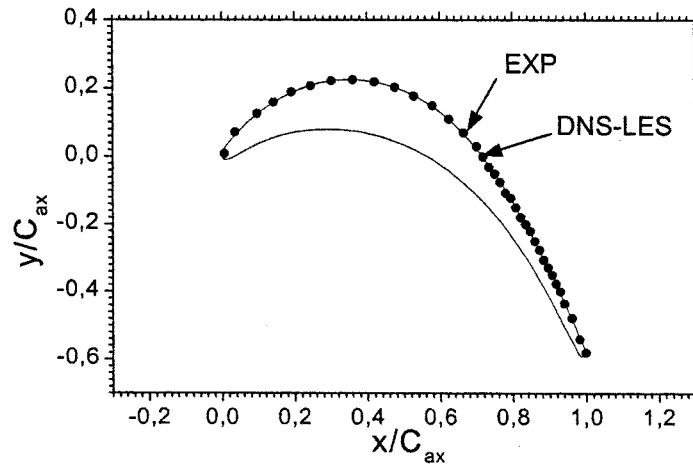
Figure 17. Location (black solid dots) of the 27 measurement stations (arrows indicate onset of intermittent separation bubble).
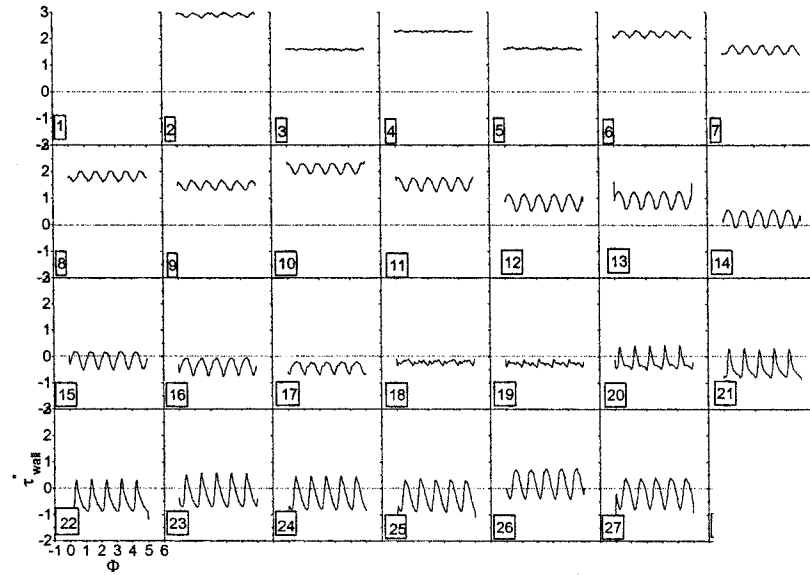

Figure 18. Measured [28] quasi-wall shear stress at 27 stations on the suction side *versus* phase.

shear stress due to problems in setting the measurement offset. Accordingly, the magnitudes of the computed values of τ_{wall} in Figures 19 and 20 have been scaled to equal approximately the time-averaged measured value. This allows the comparison of the position of the separation bubble on the suction side and the shape, but not the amplitude of the wall shear stress fluctuations. Figure 18 shows no flow separation near the leading edge. Still, the relatively long distance between two
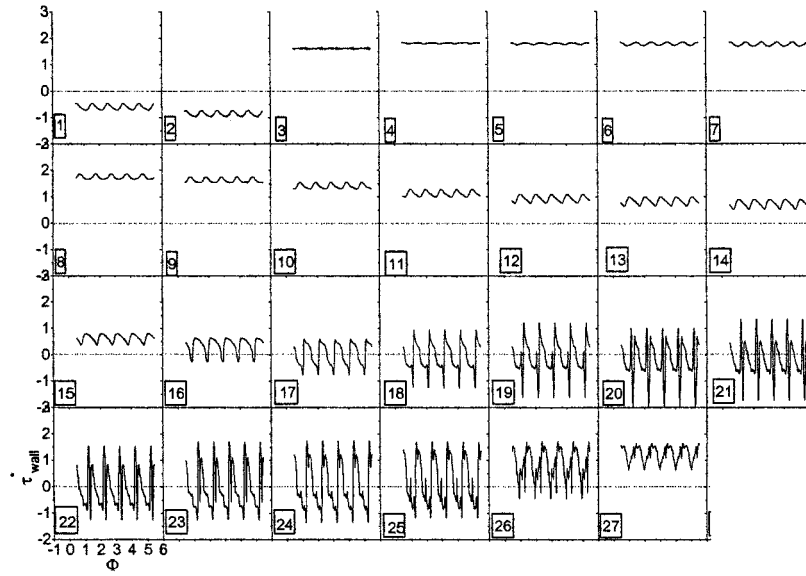
Figure 19. Scaled DNS wall shear stress at 27 stations on the suction side *versus* phase.

measurement points may indicate that the separation, if present, is not resolved. The measured C_p plotted in Figure 2 shows a small kink at $x/C_{ax} \cong 0.0677$, which might indicate the presence of a small separation bubble. This position is between the second and the third wall shear stress measurement points located at $x/C_{ax} \cong 0.036$ and 0.097 respectively. Observe that the leading edge separation might be affected by the mentioned uncertainties in the experimental inlet flow angle. Various RANS simulations have shown a long leading edge separation at an inflow angle of $\beta_1 = 45.5$. The separation bubble disappeared, however, at $\beta_1 = 43.0$.

Figures 19 and 20 show the scaled wall shear stress computed by DNS and LES respectively. In both DNS and LES section 1 is permanently separated and the incoming wake only modulates the shear stress signal. At section 2 the DNS still shows permanent separation, while in the LES the flow is attached. This is another indication that the size of the leading edge separation bubble found in the LES is shorter than the one found in the DNS, as already mentioned when discussing the phase-averaged wall shear stress.

The recovery region downstream of the first separation bubble close to the leading edge behaves very similarly for DNS and LES. Both reach almost the same value of the wall shear stress at approximately the same distance from the leading edge. This is yet another confirmation that it is the favourable pressure gradient which plays a key role along the front part of the blade, thereby suppressing any sort of turbulence activity and overruling any differences between DNS and LES.

Downstream of the second separation point, located between the 15th and 16th measurement station, the evolution in time of τ_w^* predicted by DNS and LES is
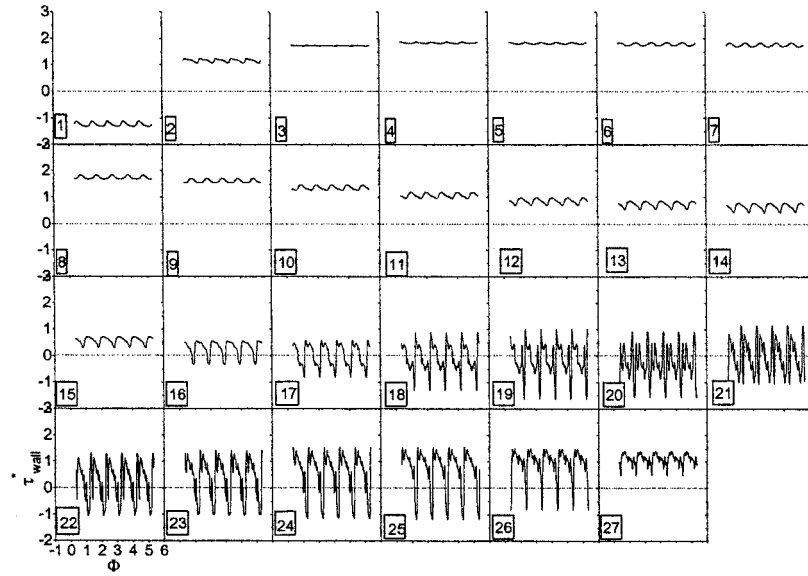
Figure 20. Scaled LES wall shear stress at 27 stations on the suction side *versus* phase.
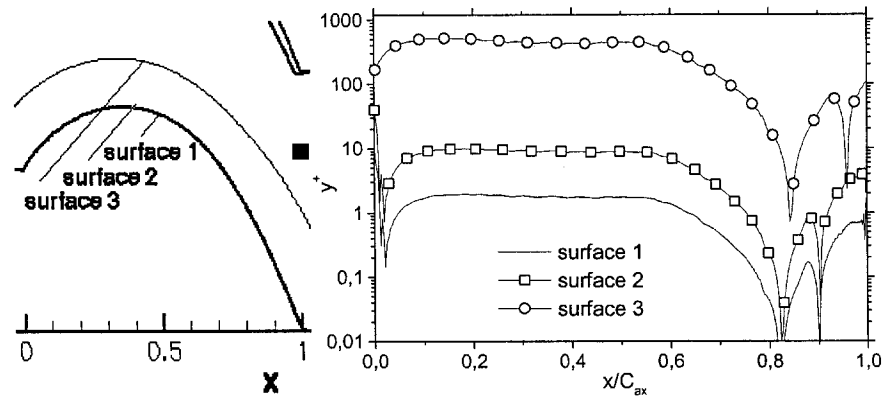

Figure 21. Non-dimensional distance from the suction side of the monitoring surfaces.

very similar, although the DNS profiles show some higher frequency content lost in the LES. Both simulations predict the onset of the separation point somewhat downstream of the measurements (point 14 in the measurements against point 16 in the simulations), and a tendency to reduce the strength of the reverse flow while approaching the trailing edge.

6.4. DETAILS ON THE SUCTION SIDE SEPARATION BUBBLES

The measurement plot of Figure 18 shows that the flow is intermittently separated already at the 14th point, corresponding to $x/C_{ax} \cong 0.66$. In the region $0.70 <$
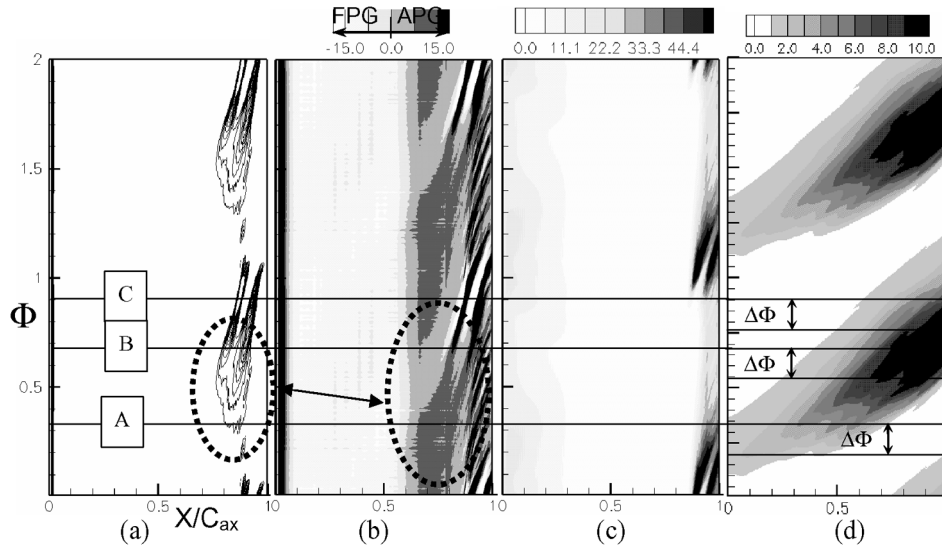
Figure 22. Phase-averaged reverse flow on surface 1 (a), acceleration parameter $\lambda_s \times 100$ (b), turbulence kinetic energy $k \times 1000$ on surface 2 (c) and on surface 3 (d) on the suction side *versus* Φ.

$x/C_{ax} < 0.99$ the measurements and both DNS and LES indicate the presence of a stalled flow region. DNS and LES predict an intermittent flow separation at $x/C_{ax} \cong 0.72$–0.73, which is slightly downstream of the measurements. In an attempt to explain the dynamics of the suction side-separation and reattachment, the flow field is analysed in time along three surfaces in the proximity of the side wall. The location of the surfaces, shown in Figure 21, has been selected to be deep inside the boundary layer (surfaces 1 and 2), and outside the boundary layer to detect the passing wakes (surface 3). Surface 1 corresponds to the first grid node adjacent to the wall. The flow is monitored using the tangential velocity, u, the fluctuating kinetic energy, k, and the suction-side acceleration parameter, λ_s, computed as

$$\lambda_s = +\theta^2_{\text{crown}} \frac{\partial p}{\partial s} \frac{\text{Re}}{U_{\text{in}}},$$

in which the momentum thickness θ is taken at the blade crown ($x/C_{ax} \cong 0.4$), and the reference velocity at the inlet. Since the shape of the contours predicted by DNS and LES is very similar, only the LES plots will be reported here.

Figure 22 shows the phase-averaged negative tangential velocity and the acceleration parameter along surface (1), together with the turbulent kinetic energy along surface (2). Figure 22a reveals the presence of a single separation bubble starting from $\Phi = A$. This bubble has moderate negative velocities and is quite thin and long. The growth of this separated flow region is directly linked to an adverse pressure gradient which extends from $x/C_{ax} = 0.65$ (shortly after the maximum

flow acceleration on the suction side), up to $x/C_{ax} = 0.8$ (see Figure 22b), as indicated by the dotted circles in Figures 22a and 22b. It is also interesting to observe that the local adverse pressure gradient is reduced by the presence of the separation bubble, which increases the displacement thickness. At $\Phi = B$, the shear layer rolls-up and generates two separate vortical structures. The large up-down values of the local acceleration parameter in the twin-bubble region suggest that the thickness of these two structures is significantly larger than that of the original separation bubble. The two vortices are convected downstream and promote a local increase of turbulence kinetic energy on surface 2 (see Figure 22c). Apparently, despite the presence of these two large structures, the flow is only weakly turbulent, and the two turbulent regions appear shortly before the reverse flow disappears and the flow reattaches at $\Phi = C$. As it was conjectured in the above paragraphs, the separation bubble appears to have a predominantly laminar nature. In summary, the flow separation is first triggered by a moderate adverse pressure gradient. The separated shear layer is very unstable and due to the triggering of a Kelvin–Helmholz instability it rolls up in two separate re-circulation bubbles in which entrained disturbances, most likely convected in the boundary layer, are fostered to promote turbulence. Provided the distance between separation and the trailing edge is sufficient, the turbulence generated in the two separation bubbles would normally settle downstream and form a turbulent boundary layer. Unfortunately in this simulation the trailing edge is too close to the location of separation and no typical turbulent boundary layer profile is obtained (see also [22, 31]).

The analysis above misses to identify the link with the incoming wakes. To be able to do this, Figure 22d shows the turbulent kinetic energy on surface (3) of Figure 21. The phase-averaged profiles of Figure 15 show that the wake reaches the suction side of the blade only marginally, probably on account of the large incidence angle. So, it is only at $y^+ \approx 500$–800 that the wake becomes clearly visible, as illustrated by the local increase in turbulent kinetic energy of Figure 22d: the wake corresponds to the dark grey region that begins at $x/C_{ax} = 0$ and ends at the trailing edge. The different pitch-wise location of surfaces (2) and (3) introduces a phase lag between the two: the wake is first felt on surface (3) and after $\Delta\Phi$ it is felt also on surface (2). The suction side boundary layer separates in the absence of any significant influence of the incoming wake ($\Phi = A$). However, the small scale velocity fluctuations convected by the wake are felt as soon as they manage to penetrate the boundary layer: the distribution of k illustrated by Figure 22d at ($\Phi = B$) corresponds to a significant thickening of the wake, the edge of which manages to reach the boundary layer. There it very likely promotes a Kelvin–Helmholz instability of the shear layer (see also [32]) causing it to roll-up to produce the two separate bubbles discussed above. Apparently, it is the wake that indirectly turns on the transition to turbulence of the boundary layer, although not much of the wake manages to penetrate the boundary layer. In other words, it is the mixed effect of these disturbances coming from outside the boundary layer, and
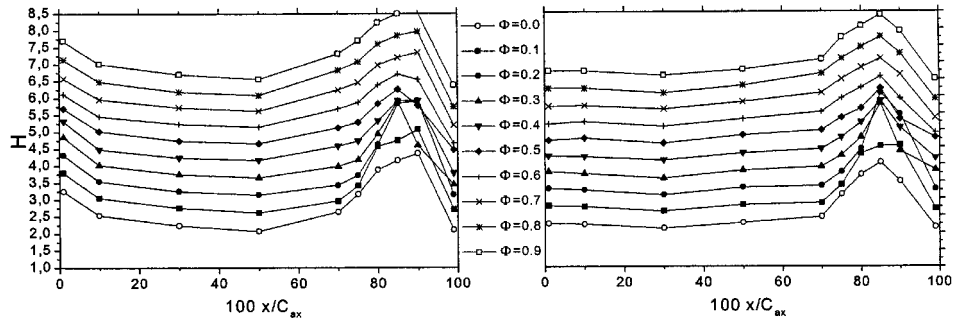
Figure 23. Shape factor along the suction side of the blade at 10 phases, left DNS, right LES (values shifted in y-direction with $\Phi \times 5$).

the local production of turbulence, that promote the turbulent reattachment of the boundary layer. This is the same picture that emerges from the flow visualisation of Wissink [31]: it is remarkable that the LES is able to capture the essential features of the flow detailed by the DNS.

6.5. BOUNDARY LAYER INTEGRAL PARAMETERS

The analysis of the cross-sections, static pressure and wall shear stress on the suction side is facilitated by plotting the integral boundary layers parameters. The computation of both the displacement and momentum thickness in unsteady separated flows is not a trivial task because of the uncertain definition of the boundary layer edge. Accordingly, a reliable procedure to compute the integral parameters from the DNS and LES results was taken from the URANS models (see [20] for further details), in which the boundary layer edge is related to the local vorticity. Figure 23 shows the shape factor, H for DNS and LES, respectively, along the suction side (only 10 points are shown, located at 1, 10, 30, 50, 70, 75, 80, 85, 90, 99% of the axial chord) for 10 different phases. The plots reveal that the integral parameters are not much influenced by the wakes, at least in the first 70–80% of the blade. A careful analysis reveals only a slight increase of δ^* for $0.4 < x/C_{ax} < 0.6$ when the wake passes over the blade wall. The two sets of profiles differ in the front part of the blade ($x/C_{ax} < 0.25$) on account of the larger separation bubble obtained in the DNS immediately downstream of the leading edge. The micro-scale velocity fluctuations found in the front part of the blade boundary layer by the DNS does not manage to promote transition to turbulence. Conversely, the further flow acceleration in both the DNS and LES, induced by the increase in the displacement thickness, raises the shape factor to values around 3.0–3.5.

Liu and Rodi [16] found much larger wake-induced disturbances in a flat plate boundary layer. However, they also measured significantly smaller perturbations in the first 50–60% of a low speed turbine boundary layer with incoming wakes [17]. The strong favourable pressure gradient encountered in the turbine flow is
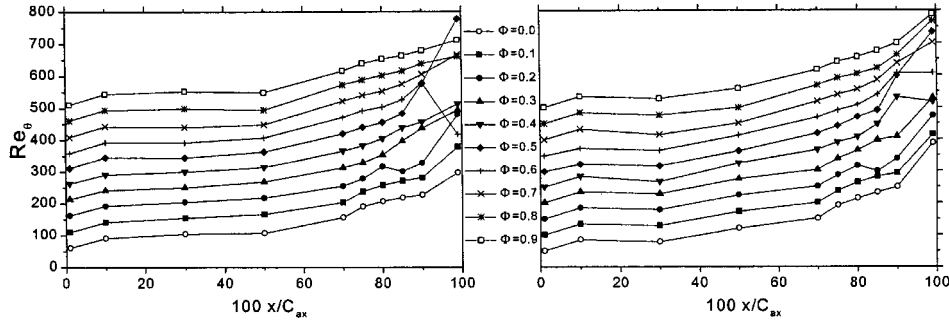
Figure 24. Re_θ along the suction side of the blade at 10 phases, left DNS, right LES (values shifted in *y*-direction with $\Phi \times 50$).

clearly the cause of such large differences. In the present case the flow turning and blade load are even larger than in [17] (100 deg against 70 deg) so that the pressure gradient is larger and consequently, the effect of impinging wake disturbances on the suction side boundary layer is smaller. For $x/C_{ax} > 0.8$ the triggering of the wake becomes evident since the shape factor fluctuates in phase with the wake. Nevertheless, *H* always remains around 2.2–2.3 for $x/C_{ax} < 0.7$ and increases around the separation point, but it never falls below 1.8–1.9 in the unstable flow region while approaching the trailing edge. In other words, as noted before, the distance between the location of the production of turbulence inside the two separation bubbles and the trailing edge of the blade is just too short for the turbulence to relax and form a typical turbulent boundary layer profile.

The Reynolds number based on the momentum thickness (Re_θ) is an important parameter in transition models. Therefore it is worthwhile monitoring Re_θ along the suction side, although Figure 22 revealed that the transition process is mainly governed by a laminar separation bubble. Figure 24 shows how the predicted Re_θ increases constantly up to $x/C_{ax} = 0.5$–06, despite the favourable pressure gradient. The large fluctuations visible in the DNS results for $x/C_{ax} > 0.9$ are most likely caused by the turbulent, wake-like flow in that region. LES shows weaker fluctuations, but this is thought to be mostly due to the reduced grid resolution.

In a further attempt to compare the temporal evolution of some quantities relevant to the suction side boundary layer, Figure 25 shows the velocity component parallel to the wall at the boundary layer edge (u_δ), the boundary layer thickness (δ) defined as the distance from the wall where $u = 0.99 \times u_\infty$, the shape factor ($H = \delta^*/\theta$), and the turbulent kinetic energy at the boundary layer edge. The plots refer to six different axial positions: $x/C_{ax} = 0.10, 0.20, 0.60, 0.80, 0.90, 0.95$. The plot of the velocity at the boundary layer edge clearly illustrates the momentum defect transported by the wake for $x/C_{ax} = 0.10, 0.20$, and also at 0.60.

As already observed by Wu and Durbin [33] at a larger Reynolds number, the velocity defect found upstream of the leading edge is converted to an excess due
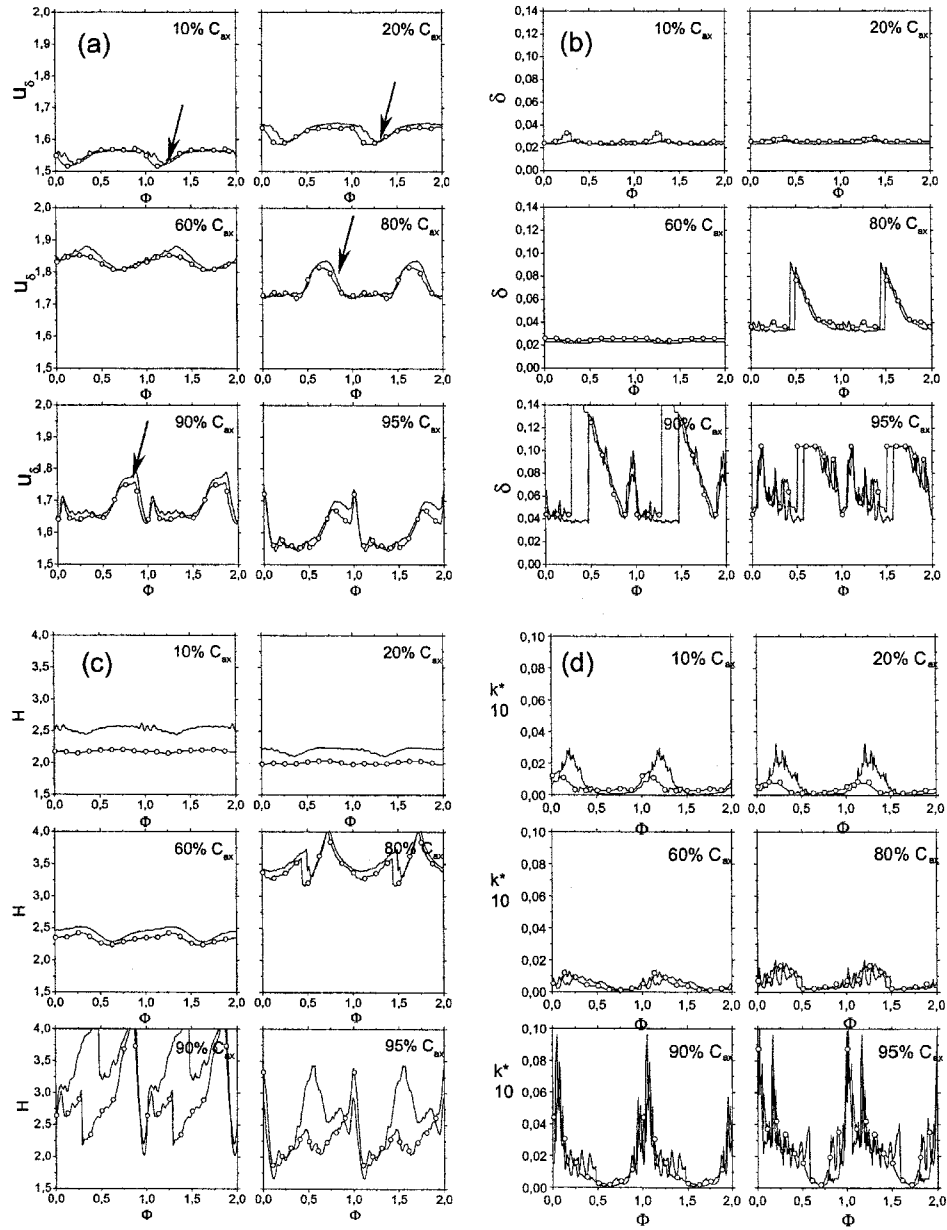
Figure 25. Time evolution of (a) velocity parallel to the wall at the boundary layer edge (u_δ), (b) boundary layer thickness (δ), (c) shape factor ($H = \delta^*/\theta$), and (d) turbulent kinetic energy, k/U_0^2 at the boundary layer edge at 10, 20, 60, 80, 90, 95% of the axial chord: solid line DNS, solid line+symbols LES.
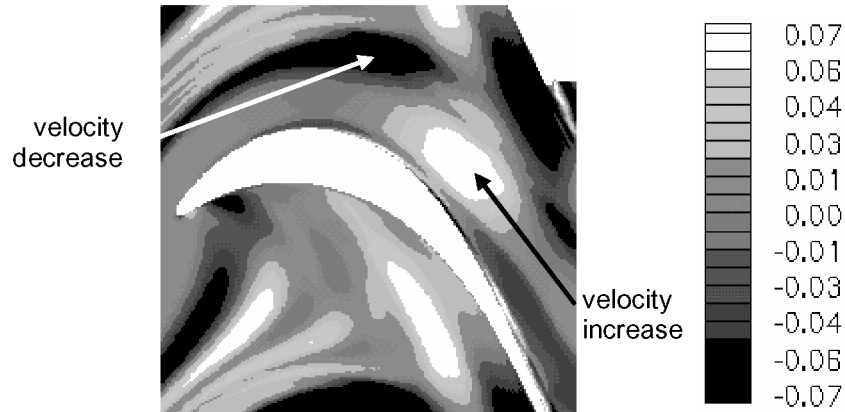
Figure 26. Typical velocity defect plot in proximity of the suction side of the blade.

to the concerted effect of the base flow turning and of the wake. This phenomenon is illustrated by the velocity defect plot of Figure 26 which indicates the alternate decrease/increase of the velocity in the wake while being swallowed into the blade vane (the velocity defect is defined as the difference between the phase-averaged and time-averaged velocity magnitude).

This is quite evident when looking at the velocity at the boundary layer edge for $x/C_{ax} \geq 80\%$; the arrows in the plots indicate the position of the wake. For $x/C_{ax} = 0.80$, the cross-analysis of Figures 25a and 22 illustrates that the peak in u_δ may be partially caused by the development of a separation bubble which provokes a flow acceleration in the outer part of the boundary layer (see $\Phi = 0.5$–0.6). This phenomenon appears again, although slightly shifted in time, for $x/C_{ax} = 0.90$. For $x/C_{ax} = 0.95$ the velocity decreases and the fluctuation range increases on account of the effect of the flow pulsation induced by the flow separation. In general, the predictions of LES are quite similar to the DNS results.

Figure 25b shows the boundary layer thickness, δ, *versus* Φ for the same six cross-sections. The presence of the wake is seen to alter the boundary layer only slightly for $x/C_{ax} < 0.60$, although a marginal increase of the boundary layer thickness is observed for $x/C_{ax} = 10$–20% for the same phase values corresponding to a local velocity defect. The minimum disturbance is found at 60% of the axial chord, which is right at the end of the strong core flow acceleration, and approximately where the wake starts to align with the direction of stretching. The large spikes visible at $x/C_{ax} = 0.8$ for $\Phi = 0.5$ are linked to the onset of separation and are in phase with u_δ. The plots also show a high frequency content for $x/C_{ax} > 0.8$.

The shape factor value, given in Figure 25c, can be determined accurately only for $x/C_{ax} < 0.8$ because of the presence of the separation bubble beyond this point, although its trend is probably correct. The differences between the DNS and LES results for $x/C_{ax} \leq 0.2$ are most likely due to the larger leading edge

separation in the former. In general, the shape factor obtained in the DNS is always slightly larger than that of the LES. The boundary layer remains laminar for most of the suction side. The transition to a typical turbulent boundary layer profile is not complete at $x/C_{ax} = 0.95$, where H reaches the lowest value of 1.8 (this agrees with the shape of the velocity profile, which is never fully logarithmic). It is interesting to observe that for $x/C_{ax} = 0.8$ and 0.9 the shape factor considerably increases for those phases at which the velocity near the boundary layer edge increases.

The plot of the turbulent kinetic energy, made non-dimensional with respect to the square of the inlet velocity (see Figure 25d) shows that the strong flow acceleration in the front part of the blade damps most of the turbulence content of the wake. This effect is best visible in the DNS and agrees with what was observed for the same blade at a larger Reynolds number by Wu and Durbin [33] as well as for a low speed turbine inlet guide vane in the experiments by Liu and Rodi [17]. It is also quite interesting to observe that the largest values of k are found for $\Phi \cong 1.1$–1.3 at $x/C_{ax} = 0.80$, which is shortly after the flow reattachment. This feature corroborates the hypothesis of a laminar separation bubble and a turbulent reattachment. Moving downstream, the turbulent kinetic energy level increases further. The shape factor illustrates that the velocity profile never reaches a logarithmic shape, i.e. a fully developed turbulent profile ($H \cong 1.4$–1.5). Nevertheless, the turbulent kinetic energy is shown to increase considerably while approaching the trailing edge. The peaks in k correspond to turbulence produced in the two re-circulation regions that appear due to a Kelvin–Helmholtz instability of the separated boundary layer discussed before. In the absence of the laminar separation, k is nearly zero. These lowermost values of the turbulent kinetic energy are reached in between two consecutive wakes, when the incoming turbulence level is close to zero in both DNS and LES (see $0.5 < \Phi < 1$ for $x/C_{ax} = 0.9$ and $0.6 < \Phi < 0.7$ for $x/C_{ax} = 0.95$). Although the velocity profile is not logarithmic, there exists considerable fine scale motion for $x/C_{ax} > 0.8$, like the one found in the DNS (see also [31]).

7. Conclusions

The flow in a low-speed linear turbine cascade with incoming wakes revealed a number of interesting phenomena, which were captured by both DNS and LES. The relatively low Reynolds number of 5.18×10^4 allowed both the direct numerical simulation and the large eddy simulation to be carried out with a reasonable computational effort. The comparison of the results showed that LES gives a fair reproduction of the DNS with a reduction of the overall computing time by a factor 10 approximately. The detailed analysis of the flow field indicated several features, some of which were already observed in [33] for a DNS at a higher Reynolds number. The main features observed are as follows:

- The flow visualisation showed that the LES was able to reproduce the elongated flow structures stemming from the interaction of the incoming wake vorticity and the stream-wise pressure gradient in the blade vane. These structures along the pressure side, also found in the DNS (see also [31]) and by Wu and Durbin at a higher Reynolds number [33], are quite strong and have a long lifespan.

- The dynamic SGS model is able to predict the behaviour of the suction side boundary layer in fair agreement with DNS, although the importance of the model is limited on account of the small values of the eddy viscosity predicted in the blade vane. Apparently the periodically appearing and disappearing suction side separation is captured with good accuracy by LES. The unavailability of detailed experimental data on the blade suction side prevents any detailed comparison with experiments. Nevertheless, the measured quasi-wall shear stress compares favourably with the simulations.

- The boundary layer undergoes a laminar separation which is intermittently suppressed by the incoming wakes. In the LES, as in the DNS, the separated shear layer is found to roll up in two separate bubbles due to a Kelvin–Helmholtz instability. Shortly after, the shear layer becomes turbulent and reattaches. The phase-averaged turbulence intensities and the analysis of the integral parameters for both DNS and LES suggests that the transition to a typical turbulent boundary layer is not complete. This is also confirmed by the *a-priori* testing of a correlation for the onset of transition. Transition is governed by two phenomena. First, the presence of the flow reversal in the absence of impinging wakes is an indication of laminar separation transition; second, periodically incoming small-scale disturbances convected by the wakes suppress separation and thus promote boundary layer reattachment.

- The strong flow acceleration in the first half of the blade is responsible for the very weak impact of the incoming wakes on the suction side boundary layer. Therefore, the suction side boundary layer behaves differently from what was discovered in flat plate experiments, in which the incoming wakes were found to promote transition shortly after the leading edge.

In conclusion, the results show that LES provides a fairly accurate representation of the flow details and compares favourably with DNS for the test case at fairly low Re considered. Although this test case cannot provide data for real turbine operating conditions, in which the by-pass transition is the dominant phenomenon, it can be used to test existing separation-bubble transition models in unsteady wake-affected accelerating boundary layers.

Further simulations of higher Reynolds number flows is and will be mainly carried out by LES and for Re = 148000 results are available already [24]. The increased value of the Reynolds number promotes by-pass transition triggered by the incoming wakes and the available data, once their accuracy is confirmed, will be used to tune and/or develop transition models for RANS calculations.

Acknowledgements

References

1. Abu-Ghannam, B.J. and Shaw, R., Natural transition of boundary layers – The effects of turbulence, pressure gradient and flow history. *Journal of Mechanical Engineering Science* **22** (1991) 213–228.
2. Adamczyk, J.J., Model equation for simulating flows in multistage turbomachinery. ASME Paper No. 85-GT-226 (1985).
3. Bräunling, W., Quast, A. and Dietrichs, H.-J., Detection of separation bubbles by infrared images in transonic turbine cascades. ASME Paper 88-GT-33 (1988).
4. Breuer, M. and Rodi, W., Large eddy simulation for complex turbulent flows of practical interest. In: Hirshel, E.H. (ed.), *Flow Simulation with High Performance Computers II*, Notes on Numerical Fluid Mechanics. Vieweg Verlag, Braunschweig (1996) pp. 258–274.
5. Cho, N.-H., Liu, X., Rodi, W. and Schönung, B., Calculation of wake-induced unsteady flow in a turbine cascade. *Journal of Turbomachinery* **115** (1993) 675–686.
6. Dénos, R., Arts, T., Paniagua, G., Michelassi, V. and Martelli, F., Investigation of the unsteady rotor aerodynamics in a transonic turbine stage. *ASME, Journal of Turbomachinery* (to appear).
7. Denton, J.D. and Singh, U.K., *Time Marching Methods for Turbomachinery Flow Calculations*. Von Karman Institute for Fluid Dynamics Lecture Series on Application of Numerical Methods to Flow Calculations in Turbomachines, Vol. 7 (1979).
8. Durbin, P.A., On the $k-\varepsilon$ stagnation point anomaly. *International Journal of Heat and Fluid Flow* **17** (1996) 89–90.
9. Emunds, R., Jennions, I.K., Bohn, D. and Gier, J., The computation of adjacent blade-row effects in a 1.5-stage axial flow turbine. *ASME, Journal of Turbomachinery* **121** (1999) 1–10.
10. Germano, M., Piomelli, U., Moin, P. and Cabot, W.H., A dynamic subgrid-scale eddy viscosity model. *Physics of Fluids A* **3**(7) (1991) 1760–1765.
11. Halstead, D.E., Wisler, D.C., Okiishi, T.H., Walker, G.J, Hodson, H.P. and Shin, H.W., Boundary layer development in axial compressors and turbines part 3 of 4: LP turbines. *Journal of Turbomachinery* **119** (1997) 225–237.
12. Harvey, N.W., Cox, J.C., Schulte, V., Howell, R. and Hodson, H.P., The role of research in the aerodynamic design of advanced low-pressure turbine. In: *Proceedings of the 3rd European Conference on Turbomachinery* (1999) pp. 123–132.
13. Hsu, K. and Lee, L., A numerical technique for two-dimensional grid generation with grid control at all of the boundaries. *Journal of Computational Physics* **96** (1991) 451–469.
14. Jeong, J. and Hussain, F., On the identification of a vortex. *Journal of Fluid Mechanics* **285** (1995) 69–94.

15. Kwon, O.K. and Pletcher, R.H., Prediction of incompresible separated boundary layers including viscous-inviscid interaction. *ASME, Journal of Fluids Engineering* **101** (1979) 466–472.
16. Liu, X. and Rodi, W., Experiments on transitional boundary layers with wake-induced unsteadiness. *Journal of Fluid Mechanics* **231** (1991) 229–256.
17. Liu, X. and Rodi, W., Velocity measurements of wake-induced unsteady flow in a linear turbine cascade. *Experiments in Fluids* **17** (1994) 45–48.
18. Mayle, R.E., The role of laminar-turbulent transition in gas turbine engines. ASME Paper 91-GT-261 (1991).
19. Mellen, C.P., Fröhlich, J. and Rodi, W., Computations for the European LESFOIL project. In: Krause, E. and Jäger, W. (eds.), *Scientific Computation in 2000*, Springer-Verlag, Berlin (2001) pp. 389–398.
20. Michelassi, V., Martelli, F., Dénos, R., Arts, T. and Sieverding, C.H., Unsteady heat transfer in stator-rotor interaction by two equation turbulence model. *ASME Journal of Turbomachinery* **121** (1999) 436–447.
21. Michelassi, V., Rodi, W. and Giess, P.-A., Experimental and numerical investigation of boundary-layer and wake development in a transonic turbine cascade. *Aerospace Science and Technology Journal* **3** (1998) 191–204 (also *IGTI Conference*, Orlando, FL, 1997).
22. Michelassi, V., Wissink, J. and Rodi, W., Analysis of DNS and LES of a low-pressure turbine blade with incoming wakes and comparison with experiments. Report No. 789, Institute for Hydromechanics, University of Karlsruhe, Germany (2002).
23. Michelassi, V., Wissink, J. and Rodi, W., DNS, LES, and URANS of periodic unsteady flow in a LP turbine cascade: A comparison. In: *Proceedings 5th European Conference on Turbomachiney Fluid Dynamics and Thermodynamics*, Prague, Czech Republic, March 18–21 (2003) (submitted).
24. Michelassi, V., Wissink, J., Fröhlich, J. and Rodi, W., LES of flow around a low pressure turbine blade with incoming wakes at realistic operating conditions. *AIAA Journal* (submitted).
25. Rhie, C.M., Gleixner, A.J., Spear, D.A., Fishberg, C.J. and Zacharias, R.M., Development and application of a multistage Navier–Stokes solver: Part I. Multistage modeling using bodyforces and deterministic stresses. *ASME, Journal of Turbomachinery* **120** (1998) 205–214.
26. Rodi, W. and Schönung, B., Interaktives-Inverses Grenzschichtverfahren zur Berechnung von lokalen Ablöseblasen an Turbinenschaufeln. *Zeitschrift für Flugwissenschaft und Weltraumforschung* **11** (1987) 271–280.
27. Savill, A.M., By-pass transition using conventional closures. In: Launder, B. and Sandham, N. (eds.), *Closure Strategies for Turbulent and Transitional Flows*. Cambridge University Press, Cambridge (2002).
28. Stadtmüller, P., Investigation of wake-induced transition on the LP turbine cascade T106A-EIZ. DFG-Verbundproject Fo 136/11, Version 1.0 (2001).
29. Stadtmüller, P., Investigation of wake-induced transition on the LP turbine cascade T106A-EIZ. DFG-Verbundproject Fo 136/11, Version 1.1 (2002).
30. Wilcox, D.C., Reassessment of the scale-determining equation for advanced turbulence models. *AIAA Journal* **26** (1988) 1299–1310.
31. Wissink, J.G., DNS of a separating low Reynolds number flow in a turbine cascade with incoming wakes. In: Rodi, W. and Fueyo, N. (eds.), *Engineering Turbulence Modelling and Experiments*, Vol. 5. Elsevier, Amsterdam (2002) pp. 731–740.
32. Wissink, J.G. and Rodi, W., DNS of transition in a laminar separation bubble. In: Castro, I.P., Hancock, P.E. and Thomas, T.G. (eds.), *Advances in Turbulence IX, Proceedings of the Ninth European Turbulence Conference*, Southampton (UK), 2–5 July, 2002. CIMNE, Barcelona (2002) pp. 727–730.

33. Wu, X. and Durbin, P.A., Evidence of longitudinal vortices evolved from distorted wakes in a turbine passage. *Journal of Fluid Mechanics* **446** (2001) 199–228.

34. Wu, X., Jacobs R.G., Hunt J.C.R. and Durbin P.A., Simulation of boundary layer transition induced by periodically passing wakes. *Journal of Fluid Mechanics* **398** (1999) 109–153.